Nanofocusing in circular sector-like nanoantennas

Zenin, Volodymyr; Pors, Anders Lambertus; Han, Zhanghua; Eriksen, René Lynge; Volkov, Valentyn S.; Bozhevolnyi, Sergey I.

Published in:
Optics Express

Publication date:
2014

Document version
Final published version

Citation for pulished version (APA):
Zenin, V., Pors, A. L., Han, Z., Eriksen, R. L., Volkov, V. S., & Bozhevolnyi, S. I. (2014). Nanofocusing in circular sector-like nanoantennas. Optics Express, 22(9), 10341-10350.

Nanofocusing in circular sector-like nanoantennas

Vladimir A. Zenin,[1,*] **Anders Pors,**[1] **Zhanghua Han,**[1,2]
René L. Eriksen,[1] **Valentyn S. Volkov,**[1] **and Sergey I. Bozhevolnyi**[1]

[1]*Department of Technology and Innovation, University of Southern Denmark, Niels Bohr Allé 1, DK-5230 Odense, Denmark*
[2]*Center for Terahertz Research, China Jiliang University, Hangzhou 310018, China*
[*]*zenin@iti.sdu.dk*

Abstract: Gold circular sector-like nanoantennas (with a radius of 500 nm and a taper angle of 60°, 90°, and 120°) on glass are investigated in a near-infrared wavelength range (900 - 2100 nm). Amplitude- and phase-resolved near-field images of circular sector-like antenna modes at telecom wavelength feature a concentric circular line of phase contrast, demonstrating resonant excitation of a standing wave of counter-propagating surface plasmons, travelling between a tip and opposite circular edge of the antenna. Transmission spectra obtained in the range 900 - 2100 nm are in good agreement with numerical simulations, revealing the main feature of this antenna configuration, viz., the resonance wavelength, in contrast to triangular antennas, does not depend on the taper angle and is determined only by the sector radius. This feature together with a robust and easily predictable frequency response makes circular sector-like nanoantennas very promising for implementing bowtie antennas and attractive for many applications.

OCIS codes: (180.4243) Near-field microscopy; (240.6680) Surface plasmons.

References and links

1. W. Zhang, L. Huang, C. Santschi, and O. J. F. Martin, "Trapping and sensing 10 nm metal nanoparticles using plasmonic dipole antennas," Nano Lett. **10,** 1006–1011 (2010).
2. M. L. Juan, M. Righini, and R. Quidant, "Plasmon nano-optical tweezers," Nature Photonics **5,** 349–356 (2011).
3. A. Weber-Bargioni, A. Schwartzberg, M. Schmidt, B. Harteneck, D. F. Ogletree, P. J. Schuck, S. Cabrini, "Functional plasmonic antenna scanning probes fabricated by induced-deposition mask lithography," Nanotechnology **21,** 065306 (2010).
4. J. N. Farahani, D. W. Pohl, H. J. Eisler, and B. Hecht, "Single quantum dot coupled to a scanning optical antenna: a tunable superemitter," Phys. Rev. Lett. **95,** 017402 (2005).
5. H. A. Atwater and A. Polman, "Plasmonics for improved photovoltaic devices," Nat Mater **9,** 205–213 (2010).
6. L. Tang, S. E. Kocabas, S. Latif, A. K. Okyay, D. S. Ly-Gagnon, K. C. Saraswat, and D. A. B. Miller, "Nanometre-scale germanium photodetector enhanced by a near-infrared dipole antenna," Nature Photonics **2,** 226–229 (2008).
7. J. A. Schuller, E. S. Barnard, W. Cai, Y. C. Jun, J. S. White, and M. L. Brongersma, "Plasmonics for extreme light concentration and manipulation," Nat Mater **9,** 193–204 (2010).
8. P. Bharadwaj, B. Deutsch, and L. Novotny, "Optical antennas," Adv. Opt. Photon. **1,** 438–483 (2009).
9. L. Novotny and N. F. van Hulst, "Antennas for light," Nature Photonics **5,** 83–90 (2011).
10. D. K. Gramotnev and S. I. Bozhevolnyi, "Plasmonics beyond the diffraction limit," Nature Photonics **4,** 83–91 (2010).
11. A. Pors, O. Albrektsen, I. P. Radko, and S. I. Bozhevolnyi, "Gap plasmon-based metasurfaces for total control of reflected light," Sci. Rep. **3,** 2155 (2013).

#205390 - $15.00 USD Received 24 Jan 2014; revised 16 Mar 2014; accepted 10 Apr 2014; published 22 Apr 2014

12. A. Pors and S. I. Bozhevolnyi, "Plasmonic metasurfaces for efficient phase control in reflection," Opt. Express **21,** 27438–27451 (2013).
13. D. P. Fromm, A. Sundaramurthy, P. J. Schuck, G. Kino, and W. E. Moerner, "Gap-dependent optical coupling of single "bowtie" nanoantennas resonant in the visible," Nano Lett. **4,** 957–961 (2004).
14. H. Fischer and O. J. F. Martin, "Engineering the optical response of plasmonic nanoantennas," Opt. Express **16,** 9144–9154 (2008).
15. D. K. Gramotnev, A. Pors, M. Willatzen, and S. I. Bozhevolnyi, "Gap-plasmon nanoantennas and bowtie resonators," Phys. Rev. B **85,** 045434 (2012).
16. L. Novotny, "Effective wavelength scaling for optical antennas," Phys. Rev. Lett. **98,** 266802 (2007).
17. T. Søndergaard, J. Beermann, A. Boltasseva, and S. I. Bozhevolnyi, "Slow-plasmon resonant-nanostrip antennas: analysis and demonstration," Phys. Rev. B **77,** 115420 (2008).
18. A. Pors, M. Willatzen, O. Albrektsen, and S. I. Bozhevolnyi, "From plasmonic nanoantennas to split-ring resonators: tuning scattering strength," J. Opt. Soc. Am. B **27,** 1680–1687 (2010).
19. R. Zia, M. D. Selker, and M. L. Brongersma, "Leaky and bound modes of surface plasmon waveguides," Phys. Rev. B **71,** 165431 (2005).
20. M. Schnell, A. Garcia-Etxarri, A. J. Huber, K. B. Crozier, A. Borisov, J. Aizpurua, and R. Hillenbrand, "Amplitude- and phase-resolved near-field mapping of infrared antenna modes by transmission-mode scattering-type near-field microscopy," J. Phys. Chem. C **114,** 7341–7345 (2010).
21. N. Ocelic, A. Huber, and R. Hillenbrand, "Pseudoheterodyne detection for background-free near-field spectroscopy," Appl. Phys. Lett. **89,** 101124 (2006).
22. A. Garcia-Etxarri, I. Romero, F. J. Garcia de Abajo, R. Hillenbrand, and J. Aizpurua, "Influence of the tip in near-field imaging of nanoparticle plasmonic modes: weak and strong coupling regimes," Phys. Rev. B **79,** 125439 (2009).
23. R. Esteban, R. Vogelgesang, J. Dorfmller, A. Dmitriev, C. Rockstuhl, C. Etrich, and K. Kern, "Direct near-field optical imaging of higher order plasmonic resonances," Nano Lett. **8,** 3155–3159 (2008)
24. M. Schnell, A. Garcia-Etxarri, A. J. Huber, K. Crozier, J. Aizpurua, and R. Hillenbrand, "Controlling the near-field oscillations of loaded plasmonic nanoantennas," Nature Photonics **3,** 287-291 (2009).
25. R. L. Olmon, P. M. Krenz, A. C. Jones, G. D. Boreman, and M. B. Raschke, "Near-field imaging of optical antenna modes in the mid-infrared," Opt. Express **16,** 20295–20305 (2008).
26. M. Schnell, P. Alonso-Gonzalez, L. Arzubiaga, F. Casanova, L. E. Hueso, A. Chuvilin, and R. Hillenbrand, "Nanofocusing of mid-infrared energy with tapered transmission lines," Nature Photonics **5,** 283–287 (2011).
27. P. B. Johnson and R.W. Christy, "Optical constants of the noble metals," Phys. Rev. B **6,** 4370–4379 (1972).
28. A. V. Zayats, I. I. Smolyaninov, and A. A. Maradudin, "Nano-optics of surface plasmon polaritons," Phys. Rep. **408,** 131-314 (2005).
29. T. Søndergaard and S. I. Bozhevolnyi, "Slow-plasmon resonant nanostructures: Scattering and field enhancements," Phys. Rev. B **75,** 073402 (2007).
30. K. L. Kelly, E. Coronado, L. L. Zhao, and G. C. Schatz, "The optical properties of metal nanoparticles: the influence of size, shape, and dielectric environment," J. Phys. Chem. B **107**, 668–677 (2003).
31. P. Alonso-Gonzalez, P. Albella, F. Neubrech, C. Huck, J. Chen, F. Golmar, F. Casanova, L. E. Hueso, A. Pucci, J. Aizpurua, and R. Hillenbrand, "Experimental verification of the spectral shift between near- and far-field peak intensities of plasmonic infrared nanoantennas," Phys. Rev. Lett. **110**, 203902 (2013).

1. Introduction

Plasmonic antennas enable a variety of cutting-edge applications such as nanosensors, nanomanipulation and near-field trapping techniques [1, 2], high-resolution probes for nanoimaging and information processing approaches [3, 4], improved photovoltaics [5], nanoscale photodetectors with significantly enhanced signal-to-noise ratio [6, 7], catalysis applications [7], efficient coupling of light energy to nanoscale structures, quantum dots and single molecules [8-10], plasmonic metasurfaces for control of light at the nanoscale [11, 12], etc. Among the vast variety of designs of plasmonic nanoantennas, bowtie antennas are used very often due to the simplicity of fabrication, tunability of the resonance, high localization and electrical field enhancement (FE) [13, 14]. However, the common used triangular shape of bowtie antennas may lead to partial destructive interference of the propagating plasmons, i.e., surface plasmon polaritons (SPPs), due to their different optical paths between bowtie vertex and the points on the opposite edge of the bowtie arm. This in turn leads to a generally reduced FE at the bowtie vertex and comparatively complex frequency response. On the contrary, the circular sector-like shape of nanoantennas is expected to result in the constructive SPP interference and nanofocus-

#205390 - $15.00 USD Received 24 Jan 2014; revised 16 Mar 2014; accepted 10 Apr 2014; published 22 Apr 2014

ing due to the same length of optical paths between the antenna vertex and the opposite circular edge [15]. That allows one to interpret the corresponding plasmonic resonances as being associated with the formation of standing SPPs travelling between the circular edge and vertex of the antenna. These structures should therefore behave similarly to other plasmonic resonators featuring typically a large length-to-width ratio [16-18], with the frequency response being relatively easy to predict and with considerable FE at the antenna vertex.

In this paper we demonstrate proofs of the concept of resonant FE due to standing SPPs in circular sector-like nanoantennas of the insulator-metal-insulator (IMI) configuration. Since SPPs travel synchronously from the antenna edge to its taper, the antenna can be considered as a stripe of variable width. Moreover, if the width of the stripe is much larger than the metal thickness, the mode effective index of SPP propagating on the stripe does not strongly depend on the stripe-width [19]. Therefore, the optical path length of the SPPs should not depend on the taper angle of a relatively thin circular sector-like antenna. Thus, the frequency response should not depend on the taper angle as well. However, this argument does not hold for incident light polarized in the transverse direction of the nanoantenna. Thus, comparing extinction cross-section spectra for antennas with different taper angles illuminated with the incident light of different polarizations, we provide a first proof of the concept. Moreover, the direct comparison of spectra for circular sector-like and triangular antennas with different taper angles indicates advantages of the first design.

Secondly, a standing SPP wave pattern should create a particular distribution of the out-of-plane component of the electric near-field, demonstrating a phase contrast of π rad between the two halves of the antenna, with a line of contrast having a concentric circular shape separating the two sectors. In this work, the near-field amplitude and phase distributions are investigated using a scattering-type scanning near-field optical microscope together with numerical simulations. The simulations for circular sector-like antennas agree well with experimental result, while the simulations for triangular antennas show more complicated phase profile, indicating a complex nature of antenna excitation.

Finally, as mentioned above, a circular shape of the sector-like nanoantenna should provide constructive interference of SPPs converging toward the taper vertex, with FE potentially exceeding those found for triangular-shaped antennas. As SPPs, however, are launched perpendicularly to the nanoantenna edges, circular sector-like antennas may (for linearly polarized light) reduce the SPP excitation efficiency in comparison with triangular antennas, which can limit the overall improvement in FE. In order to compare FE of antennas with both shapes, we study numerically resonant structures at 1500 nm with the emphasis on two different modes of the triangular antenna. Simulations show that one of these modes, which is associated with the SPP propagation along the edges connecting the apex with the other vertices, has FE comparable to the circular sector-like nanoantenna. Nevertheless, similar FE together with easily predicted and controlled frequency response makes circular sector-like antennas preferable to traditional triangular nanoantennas.

2. Materials and methods

In this paper we consider gold circular sector-like antennas with radius R, taper angle α, and thickness $t = 50$ nm, placed on a glass substrate [Fig. 1(a)], and compare them with triangular antennas of the same thickness, length L and taper angle α [Fig. 1(b)]. We fabricated circular sector-like antennas with $R = 500$ nm and $\alpha = 60^\circ$, 90°, and 120°, respectively, using electron-beam lithography, metal evaporation and subsequent lift-off. For each taper angle we fabricated an array of 10×10 antennas, separated by 4 μm, and investigated them in a near infrared (NIR) range of wavelengths from 900 to 2100 nm. The substrate was made of BK7 glass, which has a refractive index of $n \simeq 1.5$ for the considered NIR range.

#205390 - $15.00 USD Received 24 Jan 2014; revised 16 Mar 2014; accepted 10 Apr 2014; published 22 Apr 2014

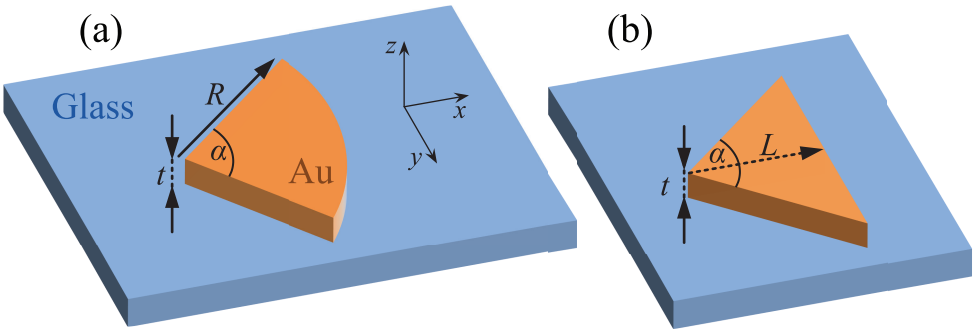

Fig. 1. Design of the (a) circular sector-like plasmonic antenna and (b) triangular antenna.

The transmission spectra of the fabricated nanoantennas were measured in an optical microscope (Olympus BX 51) where the light was sent at near normal incidence from the substrate side upwards through the sample and collected from the top using an objective with a magnification of $\times 100$ and a numerical aperture (NA) of 0.9 and analyzed in a fiber-coupled spectrometer (NIRQuest512, Ocean Optics). The light was polarized in either *x*- or *y*-direction, and the diameter of the illumination spot was around 35 μm.

Phase- and amplitude-resolved near-field investigation of nanoantennas was done using a scattering-type scanning near-field optical microscope (s-SNOM), based on an atomic force microscope (AFM), that uses cantilevered tips as near-field probes (NeaSNOM from Neaspec GmbH). In our experiments we used standard commercial Si tips covered with platinum (Arrow NCPt, NanoWorld). The sample was scanned in a tapping mode, with the tip oscillating at the mechanical resonance frequency $\Omega \approx 250$ kHz with an amplitude ~ 50 nm. The structures were illuminated from the bottom (transmission-mode, [20]) with focused light at $\lambda = 1500$ nm (the illumination spot diameter was around 3 μm). The light, scattered by the tip, was collected by a parabolic mirror and directed towards the detector, where it was overlapped with an interfering reference beam, yielding both the amplitude and the phase of the scattered light using pseudoheterodyne detection [21]. Background contributions were suppressed by demodulating the detector signal at a high harmonic frequency $n\Omega$ (in our case $n = 2$), providing background-free near-field amplitude and phase images. It should be pointed out that in most s-SNOM experiments the illumination is done in reflection-mode, where the light is focused on the tip with the same parabolic mirror that collects scattered light. This configuration creates many problems observing clear antenna modes and treatment of data due to a strong tip-sample coupling [22] and phase-retardation effects [23]. However, in our transmission-mode configuration the sample was illuminated from below, with an in-plane direction of polarization. Therefore we achieved homogeneous illumination and efficient excitation of the antenna and avoided direct excitation of the tip [20, 24]. Due to a dominating dipole moment of a tip along its axis (i.e., along *z*-axis), the recorded s-SNOM images represents mostly a distribution of the amplitude and phase of the *z*-component of the electric field, E_z [25, 26]. In order to enhance this selectivity, a polarizer at the detector was set correspondently to *z*-polarization of the light, scattered by the tip. Finally, the recorded data were imaged with free scanning probe microscopy software Gwyddion.

The transmission spectra and field distribution were simulated using the finite-element approach in the commercially available software package COMSOL MULTIPHYSICS. The values for the gold permittivity at different incident wavelengths are taken from [27]. The considered three-dimensional structures were illuminated from the bottom using a monochromatic plane wave, linearly polarized along either *x*- or *y*-axis. For all geometrical configurations, the

#205390 - $15.00 USD Received 24 Jan 2014; revised 16 Mar 2014; accepted 10 Apr 2014; published 22 Apr 2014

simulation domain was truncated using perfectly matched layers on the top and bottom facets in order to suppress artificial scattering from the truncation boundaries. On the other facets, separated by 4 μm, periodic boundary conditions were applied to simulate the array of structures. All sharp edges of antennas were rounded to 10 nm in order to avoid singular fields and to reduce the lightning rod effect [28].

3. Results and discussion

3.1. Extinction cross section

The transmission spectra for three arrays of circular sector-like antennas with taper angle of $\alpha = 60^\circ$, 90°, and 120°, respectively, were investigated with the incident light being polarized in either *x*- or *y*-direction. In order to emphasize wavelength-dependent features, an extinction cross section σ_{ext} was calculated as follows:

$$\sigma_{\text{ext}} = A(1-T), \tag{1}$$

where A is a 4×4 μm^2 unit area and T is the transmission. The results for *x*-polarization show similar frequency response for all three taper angles, with the resonance being at $\lambda \sim 1500$ nm for all configurations [Fig. 2(a)]. On the contrary, the results for *y*-polarization show strong dependence on the taper angle in the frequency response. Therefore, one can conclude, that for *x*-polarization the effective resonator length is virtually not changing with the increase of taper angle, but increases considerably for *y*-polarization, where the position of the resonance moves substantially (for $\alpha = 90^\circ$ it is at $\lambda \sim 1900$ nm, and for $\alpha = 120^\circ$ it is even beyond the measurement range). For a particular taper angle of 60° the extinction spectra for *x*- and *y*-polarization look almost the same, which is expected for the structure with a shape close to an equilateral triangle.

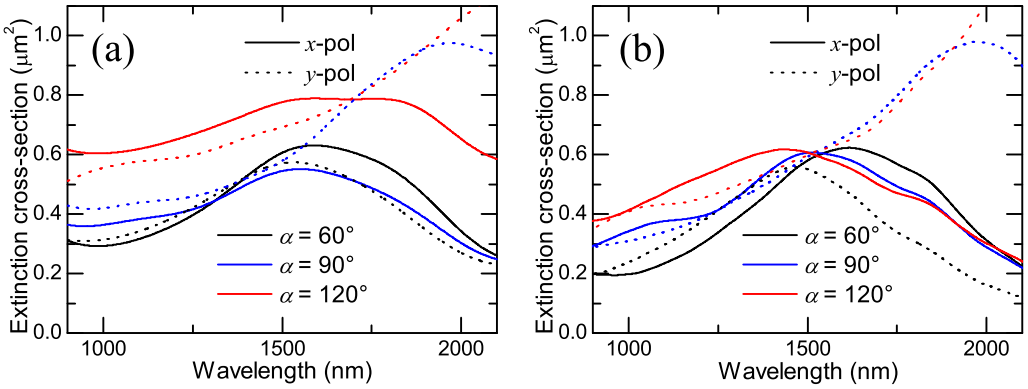

Fig. 2. (a) Experimental and (b) numerically calculated extinction cross section of *x*- (solid lines) and *y*-polarized light (dotted lines) for circular sector-like antennas with different taper angle: $\alpha = 60^\circ$ (black), 90° (blue), and 120° (red). The radius is the same, $R =$ 500 nm.

The numerical simulations of transmission spectra and corresponding extinction cross sections [Fig. 2(b)] show a good agreement with the experimental results [Fig. 2(a)], and all features discussed above are still preserved: the position of the resonance is at $\lambda \sim 1500$ nm and do not move much for *x*-polarization (compared with *y*-polarization) with the change of taper angle. The small variations of the resonance wavelength with the increase of the taper angle can be explained by the fact that SPPs are not excited uniformly on the circular edge, while

#205390 - $15.00 USD Received 24 Jan 2014; revised 16 Mar 2014; accepted 10 Apr 2014; published 22 Apr 2014

also being generated on the radial edges, hence leading to a frequency response that is not completely angle independent. Another explanation can be that a short part of the antenna near taper, being considered as a stripe, has a relatively small width, therefore the effective mode index of supported SPP is larger than the one for wide stripe, causing a red shift for the resonance wavelength of antennas with smaller taper angles. Also the phase shift acquired upon reflection of the SPP at the taper and the edge of antenna [29] might depend on the taper angle. As for the differences with experimental results, such as the level of average extinction, they can be attributed to the imperfections of fabricated structure. Noticeable red shift and an increased extinction cross-section for the measurements of 120-degrees antennas we explain by a slightly larger radius, which will be supported later by topographical images of structures.

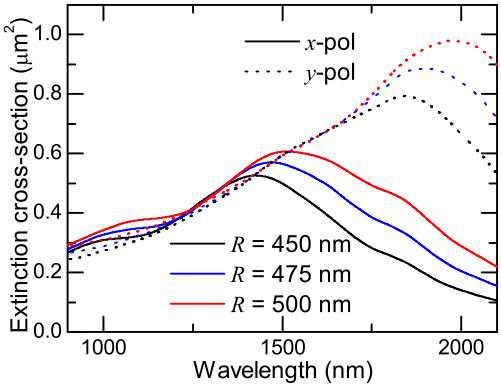

Fig. 3. Numerically calculated extinction cross section of *x*- (solid lines) and *y*-polarized light (dotted lines) for circular sector-like antennas with different radius: $R = 450$ nm (black), 475 nm (blue), and 500 nm (red). The taper angle is the same, $\alpha = 90^\circ$.

The numerical simulations were also conducted for different radii of the structures, keeping the taper angle fixed at $\alpha = 90^\circ$ [Fig. 3]. The results show a well predicted behavior of the frequency response: with the increase of radius R the resonator length increases, increasing the resonance SPP wavelength (which should fit into the resonator), therefore the resonance wavelength is also increasing. The average extinction cross section increases with the increase of the radius R, which is expected, since both scattering and absorption cross section increases.

3.2. Near-field investigations

Near-field imaging of the SPP modes of circular sector-like antennas was performed with an s-SNOM at $\lambda = 1500$ nm wavelength with either *x*- or *y*-polarized light incident from the bottom. Due to the pseudoheterodyne detection we managed to obtain both background free amplitude and phase of the out-of-plane electric near-field component, E_z [Figs. 4(a) and (c)]. Numerical simulations of the E_z field distribution at a distance of 5 nm above the structure correspond well with the experimental measurements [Fig. 4(b)]. One can see that for *x*-polarized incident light (the polarization is shown with arrows) the amplitude images show two local maxima: a hot spot at the vertex of antenna and much weaker and broader spot at the opposite edge of antenna. Due to imperfections and larger taper rounding in fabricated structure, the measured hot spot in the vertex of antenna is weaker in localization, compared to the simulation results. Also the phase measurements show some distinctions from the simulation outside the structure [the borders of the structure are shown with black lines in Fig. 4(b)], which can be explained by the residual background and tip-sample interaction presented in the experiment. Please note that only simulation results were normalized to the same color bar representing field amplitudes,

#205390 - $15.00 USD Received 24 Jan 2014; revised 16 Mar 2014; accepted 10 Apr 2014; published 22 Apr 2014

since the setup was readjusted each time before the measurement without calibration.

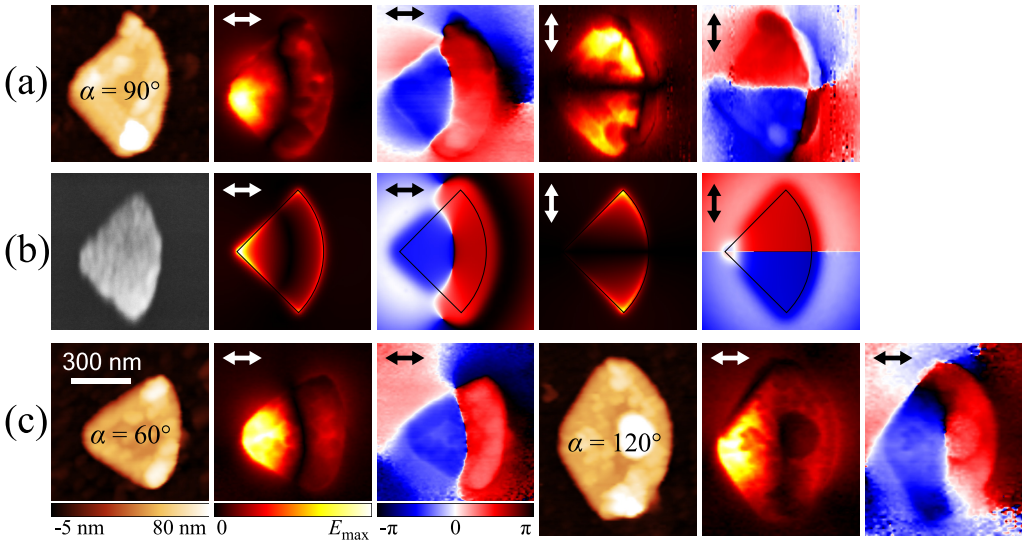

Fig. 4. (a) Pseudocolor s-SNOM images for the circular sector-like antenna with $R = 500$ nm and $\alpha = 90^\circ$ at $\lambda = 1500$ nm, showing (from left to right) topography, optical amplitude and phase for *x*- and *y*-polarized incident light. (b) Scanning electron microscope (SEM) image of the same structure as in (a), and numerically calculated distributions of E_z amplitude and phase for *x*- and *y*-polarized incident light for the same structure. (c) Pseudocolor s-SNOM images of topography, optical amplitude and phase for the antennas with $R = 500$ nm and $\alpha = 60^\circ$ and 120° at $\lambda = 1500$ nm. Linear color bars for topography and optical amplitude, as well as a periodic color bar for the optical phase images are shown. Polarization is shown with arrows.

Phase images for *x*-polarization show two distinctive antenna parts, each having almost a constant phase, while the phase difference between the two parts is π rad (note that a color bar for the phase images is periodic and shown at the bottom in Fig. 4), which is a clear indication of a standing wave. Moreover, the line of contrast between these two parts has a concentric circular shape, proving the idea of a standing wave of SPP, travelling between the edge and the vertex of the antenna. Such a split of the field distribution into two opposite parts was observed for all structures (however, the structure with $\alpha = 120^\circ$ has a weaker contrast). As was assumed before, the 120-degrees antenna has slightly larger radius, which can also explain the weak phase contrast (since the antenna is not resonantly excited). The images for *y*-polarization show the usual dipole excitation, with the middle horizontal line of phase contrast (due to symmetry of the structure).

3.3. Comparison with triangular antennas

The usage of circular sector-like antennas is motivated by rather erratic frequency responses observed for triangular antennas when geometrical parameters are varied [14]. At the same time, as also mentioned in [15], the equal length between the circular-shaped edge and the vertex improves the resonant SPP nanofocusing, potentially leading to higher resonant FE as compared to triangular antennas. In this section, we numerically compare FE at the vertex of our nominal circular sector-like nanoantenna ($R = 500$ nm, $\alpha = 90^\circ$) with those for two differently-sized triangular antennas, each having a resonance at $\lambda = 1500$ nm. The two triangular antennas have the lengths $L = 375$ nm and $L = 610$ nm, respectively, and their extinction cross- sections for

#205390 - $15.00 USD Received 24 Jan 2014; revised 16 Mar 2014; accepted 10 Apr 2014; published 22 Apr 2014

x-polarized incident light and different taper angles are shown in Fig. 5(a). It is clearly seen that the spectral response strongly depends on the taper angle, with the largest triangular antenna ($L = 610$ nm, $\alpha = 120^\circ$) demonstrating a multitude of modes in the displayed spectral range. Both triangular antennas show a peak in the extinction at $\lambda \sim 1500$ nm for the taper angle $\alpha = 90^\circ$, and the field distributions of the corresponding modes are presented in Fig. 6 together with the mode of the circular sector-like antenna. It is seen that neither of the two modes of the triangular antennas feature the standing wave pattern extending over the whole antenna area (as is the case with the circular sector-like antenna mode). The mode of the small triangular antenna is related to the standing waves formed along the radial edges, creating thereby an inhomogeneous phase profile [Fig. 6(b)], that albeit somewhat resembles that of the circular sector-like antenna, resulting at the same time in strong FE at all vertices [Fig. 6(a)]. The mode of the large triangular antenna, on the other hand, represents a standing-wave resonance concentrated along the x-direction, as clearly seen in the phase profile in Fig. 6(b), which is (similar to the mode of the circular sector-like antenna) characterized by increased FE at the taper vertex [Fig. 6(a)].

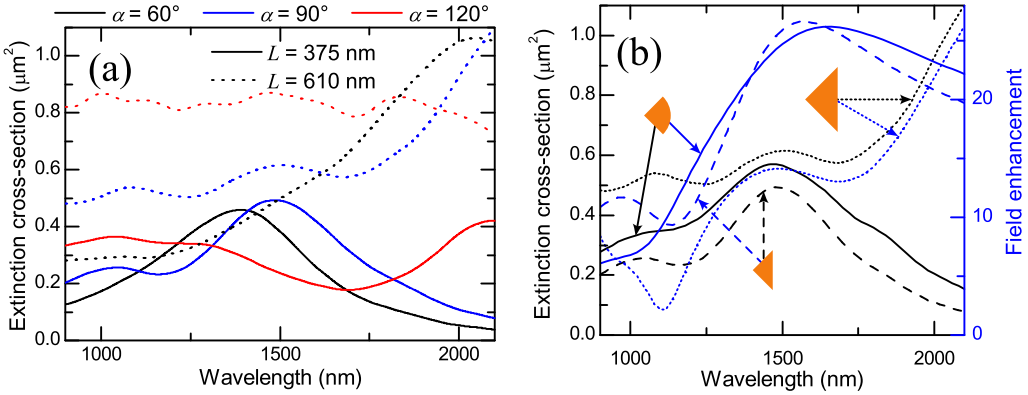

Fig. 5. (a) Numerically calculated extinction cross section of x-polarized light for small ($L = 375$ nm, solid lines) and large ($L = 610$ nm, dotted lines) triangular antennas with different taper angle: $\alpha = 60^\circ$ (black), 90° (blue), and 120° (red). (b) Comparison of circular sector-like antennas ($R = 500$ nm, solid lines) with small ($L = 375$ nm, dashed lines) and large ($L = 610$ nm, dotted lines) triangular antennas in terms of extinction cross-section (black) and field enhancement (blue).

The FE properties of the three antennas in Fig. 6 are presented in Fig. 5(b) (together with a comparison of their respective extinction cross-sections), with the FE being measured 1 nm away from the taper vertex as indicated by a green arrow in Fig. 6(c). First, it should be noted that the general redshift of the peaks in the FE (i.e., near field) spectra as compared to the extinction spectra is due to depolarization of the plasmonic mode and expected to be found for any nanoantennas with sizes not vanishingly small with respect to the wavelength [30, 31]. Secondly, it is seen that the two competing processes of efficient nanofocusing and reduced excitation efficiency of SPPs for circular sector-like antennas result in similar achievable FE levels for the two types of antennas, with the FE of the triangular antenna being strongly dependent on the choice of the resonant mode. As such, the circular sector-like nanoantenna with an easily predictable and controlled frequency response seems attractive compared to conventional triangular antennas.

#205390 - $15.00 USD Received 24 Jan 2014; revised 16 Mar 2014; accepted 10 Apr 2014; published 22 Apr 2014

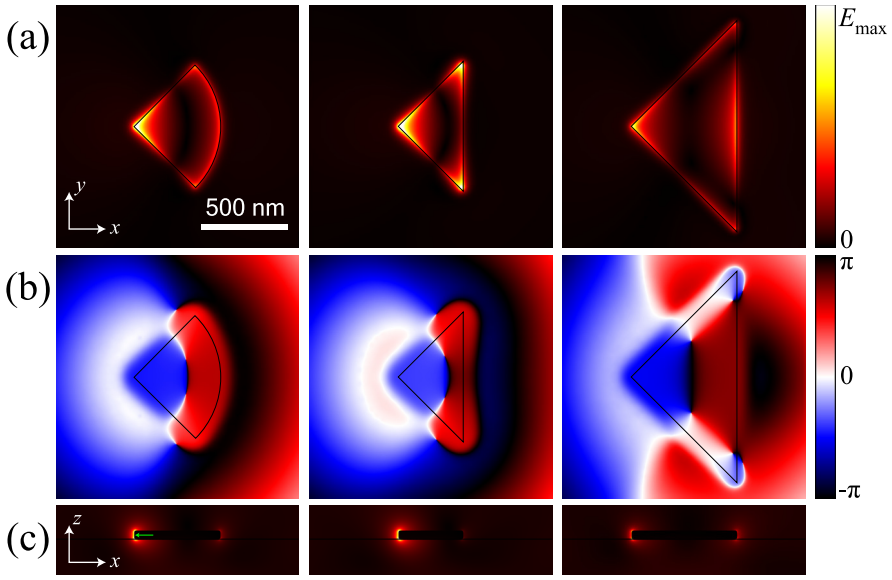

Fig. 6. E_z amplitude (a) and phase (b) of circular sector-like antennas ($R = 500$ nm, left), small ($L = 375$ nm, middle) and large ($L = 610$ nm, right) triangular antennas, numerically calculated at 5 nm above structures for x-polarized incident light at $\lambda = 1500$ nm. (c) Distributions of total field amplitude for the same types of antennas, calculated in x-z cross-section. The green arrow indicates the point used for evaluation of FE for Fig. 5(b). The top level of amplitude color bar, E_{max}, corresponds to FE of 10 for (a) and 30 for (c)

4. Conclusions

Motivated by irregular frequency responses of triangular nanoantennas with respect to changes in geometrical parameters, we have investigated circular sector-like gold nanoantenas on a glass substrate (IMI configuration) in the NIR range. It was expected that this antenna shape would lead to the constructive SPP interference at the taper of the antenna, since the SPPs excited at the antenna circular edge will have the same length of optical path to the antenna vertex, and thereby result in a more robust and predictable frequency response as well as potentially larger FE at the antenna vertex. The circular sector-like nanoantennas, described by a radius R and taper angle α, have been studied both experimentally and numerically, revealing that for light polarization along the antenna symmetry axis the extinction spectra only weakly depend on α from 60° to 120° with well-predictable behavior for changes in the sector radius. On the contrary, the extinction spectra for the opposite polarization, in which the antenna resembles a triangular antenna, varied substantially with respect to the taper angle.

Furthermore, the standing wave pattern of SPPs, travelling between the antenna taper and its circular edge, was expected to create a particular distribution of the out-of-plane electric near-field component, featuring a phase jump between two (almost) constant phase levels, having a phase difference of π rad, and bounded by a line of concentric circular shape. Such field distributions have indeed been found both experimentally and numerically for different taper angles, proving the formation of standing SPP wave.

Finally, we numerically compared the field enhancement properties of circular sector-like nanoantennas and conventional triangular antennas. Despite the nanofocusing ability of the former antenna due to standing SPPs, the circular shape simultaneously reduces the overall SPP excitation efficiency for linearly polarized light, ultimately resulting in similar levels of FE

#205390 - $15.00 USD Received 24 Jan 2014; revised 16 Mar 2014; accepted 10 Apr 2014; published 22 Apr 2014

for the two types of antennas.

We believe that the presented analysis and results obtained demonstrate convincingly that usage of the circular sector-like shape instead of triangular shape for individual antennas and their combinations (like bowtie antennas) is preferential due to more robust and easily predicted frequency responses of these nanoantennas that preserve the same attractive FE properties.

Acknowledgments

The authors thank Alexander S. Roberts and Ashwani Kumar (SDU) for having performed the SEM measurements and acknowledge support for this work from the Danish Council for Independent Research (the FTP project ANAP, Contract No. 09-072949). Z. Han also acknowledges the support from National Natural Science Foundation of China (grant 61107042).

#205390 - $15.00 USD Received 24 Jan 2014; revised 16 Mar 2014; accepted 10 Apr 2014; published 22 Apr 2014